Published in final edited form as:
J Biophotonics. 2013 June ; 6(0): 505–512. doi:10.1002/jbio.201200061.

Multimodal photoacoustic ophthalmoscopy in mouse

Wei Song[#1,4], **Qing Wei**[#1], **Liang Feng**[2], **Vijay Sarthy**[2], **Shuliang Jiao**[3], **Xiaorong Liu**[2], and **Hao F. Zhang**[1,2,*]

[1] Department of Biomedical Engineering, Northwestern University, 2145 Sheridan Rd., Evanston IL 60208, USA

[2] Department of Ophthalmology, Northwestern University, 645 North Michigan Ave., Chicago IL 60611, USA

[3] Department of Ophthalmology, University of Southern California, 1450 San Pablo Street, Los Angeles CA 90033, USA

[4] Department of Physics, Harbin Institute of Technology, 92 West Da-Zhi Street Nangang District, Harbin, Heilongjiang, P.R. China 150080

[#] These authors contributed equally to this work.

Abstract

Photoacoustic ophthalmoscopy (PAOM) is a novel imaging technology that measures optical absorption in the retina. The capability of PAOM can be further enhanced if it could image mouse eyes, because mouse models are widely used for various retinal diseases. The challenges in achieving high-quality imaging of mouse retina, however, come from the much smaller eyeball size. Here, we report an optimized imaging system, which integrates PAOM, spectral-domain optical coherence tomography (SD-OCT), and autofluorescence-scanning laser ophthalmoscopy (AF-SLO), for mouse eyes. Its multimodal capability was demonstrated by imaging transgenic Nrl-GFP mice that express green fluorescent protein (GFP) in photoreceptors. SD-OCT provided guidance of optical alignment for PAOM and AF-SLO, and complementary contrast with high depth-resolution retinal cross sections. PAOM visualized the retinal vasculature and retinal pigment epithelium melanin, and AF-SLO measured GFP-expressing in retinal photoreceptors. The *in vivo* imaging results were verified by histology and confocal microscopy.

Keywords

Photoacoustic ophthalmoscopy; optical coherence tomography; scanning laser ophthalmoscopy; retinal imaging

1.Introduction

Mouse models are widely used in biomedical research to understand mechanisms and to develop therapeutic strategies for many ocular and systemic diseases [1-3]. The advantages

[*] Corresponding author: H.F. Zhang: hfzhang@northwestern.edu.

Supporting information for this article is available free of charge under http://dx.doi.org/10.1002/jbio.[DOI]

of using mouse models for human retinal disorders is that mouse has a well-characterized genome, established techniques for genetic manipulation [1,2], and genetically defined strains, all of which are not yet available in other species. Next to human, mouse has the best annotated genome, which has high sequence conservation with the coding regions in human genome [4]. As a result, identifying links between conserved genes and specific ocular disorders in mouse models could greatly benefit understanding of human ocular diseases. Several transgenic techniques are available to alter gene functions by gene ablation, knock-in technique, or conditional mutation [5]. Moreover, cell-specific promoters can be used to label and characterize particular cell types in mouse models *in vivo* [6,7].

Currently, histologic examination remains the main method for pathological characterization in mouse models of retinal diseases, which only provides snapshot of the tissue at the time of sacrifice. If appropriate noninvasive retinal imaging technologies can be developed and applied, longitudinal monitoring of retinal disease onset and progression, as well as therapeutic response in the same animal becomes possible. As a result, it will not only reduce the number of animals used in a study, but also open up new window for investigating in *in vivo* subjects.

There are several existing technologies for mouse retinal imaging, including scanning laser ophthalmoscopy (SLO), spectral-domain optical coherence tomography (SD-OCT), and fundus camera. SLO allows fundus imaging of mouse eye [8,9]. The physiopathology information of the retina can be revealed by visualizing the retinal and choroidal vasculature anatomy and leakage with the help of contrast agents such as fluorescein and indocyanine green (ICG) [8,10], or by detecting the lipofuscin autofluorescence (AF) [8,9]. Although SLO delineates the retinal microvasculature with high transverse resolution, it has very poor axial resolution. SD-OCT, on the other hand, is capable of acquiring high axial-resolution cross-sectional images of the retina showing good agreement with histology [11,12]. Moreover, SD-OCT can measure retinal blood flow by detecting Doppler shift impinged on the reflected photons from the moving blood cells in retinal vessels [13]. However, SD-OCT is not sensitive enough to measure the retinal optical absorption properties that are closely correlated with various physiological parameters, including hemoglobin oxygen saturation (sO_2) and melanin concentration in retinal pigment epithelium (RPE). Fundus camera for mouse is commercially available [14] and can achieve very high spatial resolution through a coupling gel, which cancels the optical power of the mouse eye; however, it doesn't have axial resolution and is not sensitive to optical absorption properties.

Photoacoustic ophthalmoscopy (PAOM), developed from optical-resolution photoacoustic microscope [15,16], is specifically designed to image the optical absorption properties of the retina. PAOM delivers short laser pulses into the posterior segment of the eye and detects wide-band photoacoustic (PA) signals with an unfocused ultrasonic transducer [17]. Because hemoglobin and melanin have high molecular extinction coefficients, PAOM is able to image retinal/choroidal vessels and the RPE at a high contrast [17,18]. By adopting the well-established spectroscopic PA measurement of chromophore concentration [19-22], PAOM holds promise in mapping sO_2 in single retinal vessel. The limitations of PAOM, however, are the limited axial resolution [17] and field-of-view (FOV) [23], both of which are determined by the ultrasonic detector. Although highly sensitive to hemoglobin

concentration, PAOM currently cannot resolve retinal capillary network as fluorescein angiogram does [24] due to limited ultrasonic detecting sensitivity.

In this work, we report an optimized multimodal retinal imaging system, integrating PAOM with SD-OCT and SLO, specifically for mouse eyes. To demonstrate its capabilities, transgenic Nrl-GFP mice were imaged and compared with littermate controls. *In vivo* imaging results were verified by immunohistochemistry and confocal microscopy.

2. METHODS

2.1. Experimental setup

Figure 1 shows a schematic diagram of the mouse imaging system consisting of three subsystems: PAOM, autofluorescence SLO (AF-SLO), and SD-OCT. In the PAOM subsystem, a frequency-doubled Nd:YAG laser (SPOT-10-100, Elforlight Ltd, UK: 532-nm; 10-μJ/pulse; 2-ns pulse duration; 24-kHz pulse repletion repetition rate) was used as the illumination source. The laser light was delivered through a single mode fiber and was collimated to 3.0 mm in diameter. The output laser was scanned by a galvanometer (QS-7, Nutfield Technology) and delivered to the posterior segment of the eye with a telescope configuration (L1 and L2 in Figure 1). In order to minimize the effect of aberration due to the small eyeball size in mice [25], we used an iris to adjust the PAOM illumination laser beam on the pupil plane. By adjusting the illuminating beam diameter from 100 μm to 1 mm, we found out that a beam diameter around 400 μm gave the best balance between the aberration and numerical aperture by examining the resolved retinal vessels in the PAOM images.

The induced PA waves from the retina were detected by a custom-built unfocused needle ultrasonic transducer (40-MHz central frequency, 16-MHz bandwidth, 0.4×0.4 mm^2 active element size). The transducer was gently placed in contact with the eyelid coupled by ultrasound gel. After amplified by 40 dB (ZFL-500LN+, Mini-circuits, and 5073PR, Olympus), the PA signals were digitized by a high-speed data acquisition board (CS14200, Gage Applied) at a sampling rate of 200 MS/s. The PAOM irradiation pulse energy was about 40 nJ, which is considered to be eye-safe [17,26].

In the AF-SLO subsystem, a continuous 488-nm laser (161C-410-21, Spectra Physics, CA) was used as the excitation source. The output laser was combined with the 532-nm light by a dichroic mirror (T495lpxr, Chroma Technology Corp.), and was further combined with the SD-OCT sample arm by a hot mirror (FM02, Thorlabs). The three laser beams shared the same scanning and delivery mechanisms to radiate the mouse retina as described for PAOM above. The emitted fluorescent light passed through a long-pass filter (FEL0500, Thorlabs; cut-off wavelength: 500-nm), and was detected by an avalanche photodetector (APD110A2, Thorlabs).

The SD-OCT subsystem consists of a broadband light source (IPSDD0804, InPhenix; center wavelength: 840-nm; 6-dB bandwidth: 50-nm), a 50×50 single-mode fiber coupler, a reference arm, a sample arm coupled with the combined PAOM and AF-SLO laser beams, and a home-built spectrometer [27]. The OCT A-line rate was 24 kHz, which is the same as

the pulse repetition rate of the PAOM laser. The OCT probing light power was 0.8 mW, which is also within the ANSI laser safety limit.

The PAOM and SD-OCT were synchronized by an analogue output board (PCI-6731, National Instruments), which also triggered the PAOM laser firing and the SD-OCT image acquisition, and controlled the galvanometer scanner. A photodiode (PD in Figure 1, DET10A, Thorlabs) was used to trigger the PAOM and AF-SLO data acquisition.

2.2. Animal preparation

We imaged 8-weeks old transgenic Nrl-GFP mice in which GFP driven by the neural retina leucine zipper (Nrl) promoter [28] is specifically expressed in rod photoreceptors [29,30]. Before imaging, mice were anesthetized by intraperitoneal (i.p.) injection of a cocktail of Ketamine (87 mg/kg body weight) and Xylazine (13 mg/kg body weight). We then applied 0.5% Tetracaine Hydrochloride ophthalmic solution to paralyze the iris sphincter muscle, and 1% Tropicamide ophthalmic solution to dilate the pupil. During imaging, we applied commercial artificial tears (Systane, Alcon Laboratories, Inc.) to the eyes every other minute to prevent cornea dehydration and cataract formation. The anesthetized mice were restrained in a homemade animal holder.

To acquire images, SD-OCT and PAOM were performed simultaneously and AF-SLO was conducted thereafter due to laser safety concerns. The scanning angle in all imaging modalities was 26 degrees. The whole retinal imaging duration, including optical alignment, ultrasonic transducer orientation, and data acquisition, was less than two minutes. After experiments the mice were removed immediately from the holder and follow-up OCT examinations showed no noticeable retinal damages. All experiments were performed in compliance with the laboratory animal protocol approved by the Animal Care and Use Committee of the Northwestern University.

2.3. Histology

For histological analysis, mice were sacrificed and eyes were dissected as previously described [31]. Briefly, samples were fixed in 4% paraformaldehyde (PFA) in phosphate buffer saline (PBS) at 4 °C for 1 hour, cryo-protected in 20% sucrose in PBS, and embedded in Tissue-Tek O.C.T. (Sakura, Torrance, CA). Retinal sections were cut at a thickness of 14 μm for cryo-stat sectioning, and then stained by DAPI (4', 6-diamidino-2-phenylindole) to label all nuclei in distinct retinal layers.

To compare with the *in vivo* imaging results from GFP-expressing eyes, we performed the fluorescence microscopy of whole-mount retinal samples. Fluorescence images of the GFP-expressing photoreceptors were captured with a LSM 5 PASCAL confocal microscope (ZEISS). To better reveal the radial pattern of retinal blood vessels, we used POU4F2 (Brn-3b) antibody to label the subtype retinal ganglion cells (RGCs) [32], by which the trace of retinal vessels can be visualized in areas devoid of labeled RGCs.

3. RESULTS AND DISCUSSION

3.1. Multimodal fundus images

The multimodal fundus images of a Nrl-GFP mouse are shown in the left column of Figure 2. In the *en face* SD-OCT image (Figure 2a), the pixel intensity represents the mean intensity value along the corresponding A-line (depth scan). Membrane-rich but less optically-dense layers, such as the retinal nerve fiber layer and inner plexiform layer, have a major contribution to SD-OCT fundus image [11,12]. The retinal vessels appear dark because of strong optical absorption of hemoglobin causing less back-scattered photons from vessels.

The PAOM fundus image is shown in Figure 2b. Besides retinal vessels, PAOM also visualized the RPE at a high contrast due to the strongly optically absorbing melanin. Because RPE melanin has a much higher optical absorption coefficient at the 532-nm wavelength than that of hemoglobin [33], PA signals generated from the RPE have much higher amplitudes than those from the vessels. Hence, the retinal vessels in PAOM also appear dark. To demonstrate the volumetric imaging capability of PAOM, a movie showing the volumetric rendering of the dataset for Figure 2b is provided in the Supporting Information.

Figure 2c is the AF-SLO fundus image representing the GFP expression in the transgenic mouse. In Figure 2c, high fluorescence intensity corresponds to the rod photoreceptors expressing GFP and the dark regions represent the cone photoreceptors without GFP expression [29,30]. We can observe that the retinal regions with GFP expression are much larger than dark regions, which is because rod photoreceptors dominate in mouse retina [34]. Additionally, we can observe the shadows created by the retinal vessels blocking the 488-nm excitation light.

Although PAOM, SD-OCT, and AF-SLO have comparable lateral resolution, which is predominantly determined by the effective numerical aperture of mouse eye (only minor difference caused by different optical wavelength) and spherical aberration, PAOM demonstrated better imaging quality of the retinal vasculatures compared with the other two. In PAOM, some smaller vessels with an estimated diameter of about 20 μm or less (highlighted by the arrows in Figure 2b) can be observed. We think that the difference comes from the source of imaging contrast. In PAOM, the RPE melanin generated high-amplitude PA signals, which permitted the shadows created by the small vessels to be distinguished from the bright RPE background even though the microvessels might not be directly imaged by PAOM. SD-OCT and AF-SLO were primarily based on the optical scattering and fluorescence contrasts, respectively, and thus multiple scattering may blur the smaller vessels. Please note that, in certain situations, retinal vessels can be better resolved by SD-OCT than PAOM because of chromatic aberration and the different optical wavelengths used in these two modalities.

To compare with the GFP-expressed results, we imaged littermate control mice with no GFP expression. The results are shown in the right column of Figure 2. In both SD-OCT and PAOM (Figure 2d and Figure 2e, respectively), the fundus images in the control eye show

comparable quality with those from the GFP-expressed eye. However, AF-SLO revealed the difference. In the control eye (Figure 2f), only random noise was detected by AF-SLO, suggesting the absence of GFP expression in the retina.

Because SD-OCT and PAOM illumination lights were well aligned before the *in vivo* imaging and they shared the same delivery and scanning mechanisms, the retinal images acquired simultaneously by the two modalities are automatically registered. There was no observable eye movement when we switched the imaging system to AF-SLO mode, and, therefore, the AF-SLO image was registered with both the PAOM and OCT images.

3.2. Comparison of retinal cross sections

To further demonstrate the complementary nature among the three modalities, we compared SD-OCT B-scan, PAOM B-scan, and 1D AF-SLO profile (Figure 3). The dashed-line in Figure 2a indicates the locations of the 1D profile and B-scan images in their corresponding retinal images. The alternating bright and dark bands in SD-OCT B-scan (Figure 3a) were contributed by the different optical scattering properties in each anatomic retinal layer. Because SD-OCT predominately depends on the optical scattering property of biological tissues, it cannot image retinal vessels well, where only four shadows created by the retinal vessels were observed. In the PAOM B-scan image (Figure 3b), four retinal vessels and RPE/choroid complex were identified with a high signal-to-noise ratio (SNR) of around 35 dB due to the strong optical absorption of hemoglobin and melanin. However, no other anatomic layers can be resolved in Figure 3b because of their very low absorption coefficients [33]. Note that the current PAOM cannot distinguish the RPE from the choroid, which is abundant in vasculatures and melanin, owing to the limited axial resolution (~23 μm). To resolve RPE well, an axial resolution around one micrometer is required. The 1D profile of AF-SLO (Figure 3c) is an integration of all the emission fluorescence along the depth at each illumination spot in the retina. The low fluorescence intensities can be caused by the retinal vessels blocking the excitation laser (pointed out by arrows) as well as the photoreceptors without GFP expression. The profile peaks were contributed by the rod photoreceptors expressing GFP, where the AF intensities were locally high. Here, the axial resolution of AF-SLO was very poor because no pin-hole was used. The lateral registration among the three imaging modalities can be concluded by comparing the locations of the retinal vessels (labeled by arrows).

3.3. Histological analysis

To verify the AF-SLO results, we performed immunohistochemistry of the imaged mouse retina. The cross sections shown in Figure 4a and 4b correspond to the animals imaged in the left and right columns of Figure 2, respectively. In both eyes, the anatomic retinal layers were revealed by DAPI staining (the blue color). A turquoise band was observed overlapping with the outer nuclear layer (ONL) in Figure 4a, indicating the GFP expression in the outer retina. Dark spots (highlighted by arrows) in turquoise band represent retinal photoreceptors without GFP. In the control eye (Figure 4b), multiple retinal layers were visualized without GFP expression. The histological examinations confirmed the source of contrast in the *in vivo* AF-SLO results.

3.4. Comparison of *in vivo* and *ex vivo* whole-mount results

We also took confocal microscopy images of whole-mounted retina of the transgenic Nrl-GFP mouse (Figure 5), whose *in vivo* results are shown in the left column of Figure 2. The traces of major retinal vessels (labeled by number 1 to 10) can be observed in Figure 5a. The GFP expression was obtained by autofluorescence confocal microscopy (Figure 5b).

To compare the *in vivo* retinal images with the whole-mount results, we extracted smaller regions from the original PAOM and AF-SLO fundus images. The dashed-box in Figure 2b indicates the locations of the magnified PAOM and AF-SLO images in their original images. Since PA waves originating from multiple layers at different depths have different time-of-flight before reaching the ultrasonic transducer, the retinal vessels can be numerically segmented from RPE layer [17]. We overlaid the segmented PAOM image of retinal vessels onto the AF-SLO fundus image (Figure 5c), where the retinal vessels were pseudo-colored in red and the photoreceptors with GFP expression were pseudo-colored in green. In the combined image, the retinal vessels detected by PAOM showed a good agreement with the shadows created by these retinal vessels of AF-SLO.

Comparison between the overlaid *in vivo* image (Figure 5c) and the immunostaining counterparts (Figure 5a and 5b) suggests close correspondence in both the retinal vessels (labeled with numbers) and dark spots (cone photoreceptors, pointed by arrows).

4. CONCLUSION

Previously, we combined PAOM, SD-OCT, and SLO into a single ophthalmic imaging platform for obtaining complementary optical contrasts in rats [24]. Compared with rats, mice have a smaller eyeball size, very small pupils, and rapid cataract formation, which, in turn, cause more challenges in imaging mouse retina [12]. The much smaller pupil size of the mouse eye makes the alignment of light delivery difficult, and degrades the imaging SNR due to reduced amount of reflected photons from the retina. The cataract formation of mouse eye decreases light transmission efficiency, which may cause lower retinal imaging quality [9]. Additionally, the stronger eye aberration [25] makes imaging mouse retina considerably harder than rat retina. However, because the available tools for genetic manipulation in mice are more advanced than for rats [1,4,5], the capabilities of multimodal retinal imaging in mouse models are very attractive.

In this work, we reported the integrated PAOM, SD-OCT, and AF-SLO for the *in vivo* mouse retinal imaging. In this multimodal system, SD-OCT provided the guidance for optical alignment of PAOM and AF-SLO, and, meanwhile, resolved the micro-anatomic retinal structures at high axis-resolution (Figure 3a). PAOM is an optical-absorption based technique [17], and is ideal for imaging hemoglobin and melanin related anatomy and physiology. Hence, PAOM can potentially be applied to study age-related macular degeneration (AMD) where the melanin-rich RPE dysfunction is often considered an underlying cause of AMD [35,36]. PAOM can also be potentially applied to study ischemia-driven retinopathy [37] by measuring sO_2 in the retina. By further combining SD-OCT and PAOM with AF-SLO, anatomic and physiological information can be further correlated with specifically labeled cell types to offer great promise in more comprehensive

investigation of retinal diseases such as retinitis pigmentosa and AMD, where photoreceptors apoptosis leads to reduction of ONL [38,39].

In conclusion, being the best-understood experimental mammal, mice models are the closest surrogate for human retinal diseases. Moreover, because retinal pathophysiology is often associated with multiple optical contrasts, our integrated PAOM, SD-OCT, and AF-SLO system for mouse is expected to be an invaluable tool for fundamental investigation of human blinding diseases.

Supplementary Material

Refer to Web version on PubMed Central for supplementary material.

Acknowledgments

We thank Dr. Anand Swaroop for providing us Nrl-GFP mice and Drs. Tan Liu and Joseph Dudley for experimental assistance. We thank the generous support from the NSF CAREER CBET-1055379, NIH RC4EY021357, and NIH R01EY019951 to HFZ. We also acknowledge the support from the NIH R01EY019034 to XL, NIH R01EY019325 to VS, and the support from the China Scholarship Council to WS.

References

1. Pang, IH.; Clark, AF. Animal Models for Retinal Diseases. Humana press; New York: 2010. p. 25
2. Stahl A, Connor KM, Sapieha P, Chen J, Dennison RJ, Krah NM, Seaward MR, Willett KL, Aderman CM, Guerin KI, Hua J, Löfqvist C, Hellström A, Smith LE. Invest. Ophthalmol. Vis. Sci. 2010; 51:2813–2826. [PubMed: 20484600]
3. Takahashi H, Hirai Y, Migita M, Seino Y, Fukuda Y, Sakuraba H, Kase R, Kobayashi T, Hashimoto Y, Shimada T. Proc. Natl. Acad. Sci USA. 2002; 99:13777–13782. [PubMed: 12370426]
4. Chang B, Hawes NL, Hurd RE, Wang J, Howell D, Davisson MT, Roderick TH, Nusinowitz S, Heckenlively JR. Vis. Neurosci. 2005; 22:587–593. [PubMed: 16332269]
5. Adams DJ, Weyden L. Physiol. Genomics. 2008; 34:225–238. [PubMed: 18559964]
6. Liu X, Robinson ML, Schreiber AM, Wu V, Lavail MM, Cang J. J. Comp. Neurol. 2009; 514:449–458. [PubMed: 19350645]
7. Sarthy V, Hoshi H, Mills S, Dudley VJ. Neuroscience. 2007; 144:1087–1093. [PubMed: 17161542]
8. Seeliger MW, Beck SC, Pereyra-Muñoz N, Dangel S, Tsai JY, Luhmann UF, Pavert SA, Wijnholds J, Samardzija M, Wenzel A, Zrenner E, Narfström K, Fahl E, Tanimoto N, Acar N, Tonagel F. Vision. Res. 2005; 45:3512–3519. [PubMed: 16188288]
9. Paques M, Simonutti M, Roux MJ, Picaud S, Levavasseur E, Bellman C, Sahel JA. Vision. Res. 2006; 46:1336–1345. [PubMed: 16289196]
10. Luhmann UF, Lin J, Acar N, Lammel S, Feil S, Grimm C, Seeliger MW, Hammes HP, Berger W. Invest. Ophthalmol. Vis. Sci. 2005; 46:3372–3382. [PubMed: 16123442]
11. Fischer MD, Huber G, Beck SC, Tanimoto N, Muehlfriedel R, Fahl E, Grimm C, Wenzel A, Remé CE, Pavert SA, Wijnholds J, Pacal M, Bremner R, Seeliger MW. PLoS One. 2009; 4:e7507. [PubMed: 19838301]
12. Ruggeri M, Wehbe H, Jiao S, Gregori G, Jockovich ME, Hackam A, Duan Y, Puliafito CA. Invest. Ophthalmol. Vis. Sci. 2007; 48:1808–1814. [PubMed: 17389515]
13. Wehbe H, Ruggeri M, Jiao S, Gregori G, Puliafito CA, Zhao W. Opt. Express. 2007; 15:15193–15206. [PubMed: 19550803]
14. http://www.phoenixreslabs.com
15. Maslov K, Zhang HF, Hu S, Wang LV. Opt Lett. 2008; 33:929–931. [PubMed: 18451942]
16. Wang LV. Nat. Photonics. 2009; 3:503–509. [PubMed: 20161535]

17. Jiao S, Jiang M, Hu J, Fawzi A, Zhou Q, Shung KK, Puliafito CA, Zhang HF. Opt. Express. 2010; 18:3967–3972. [PubMed: 20389409]
18. Wei Q, Liu T, Jiao S, Zhang HF. J. Mod. Optic. 2011; 58:1997–2001.
19. Hu S, Wang LV. J. Biomed. Opt. 2010; 15:011101. [PubMed: 20210427]
20. Yao J, Maslov K, Zhang Y, Xia Y, Wang LV. J. Biomed. Opt. 2011; 16:076002. [PubMed: 21806263]
21. Liu T, Wei Q, Wang J, Jiao S, Zhang HF. Biomed. Opt. Express. 2011; 2:1359–1365. [PubMed: 21559147]
22. Razansky D, Distel M, Vinegoni C, Ma R, Perrimon N, Köster RW, Ntziachristos V. Nat. Photonics. 2009; 3:412–417.
23. Xie Z, Jiao S, Zhang HF, Puliafito CA. Opt. Lett. 2009; 34:1771–1773. [PubMed: 19529698]
24. Song W, Wei Q, Liu T, Kuai D, Burke JM, Jiao S, Zhang HF. J. Biomed. Opt. in press.
25. Geng Y, Schery LA, Sharma R, Dubra A, Ahmad K, Libby RT, Williams DR. Biomed. Opt. Express. 2011; 2:717–738. [PubMed: 21483598]
26. Hu S, Rao B, Maslov K, Wang LV. Opt. Lett. 2010; 35:1–3. [PubMed: 20664653]
27. Jiao S, Xie Z, Zhang HF, Puliafito CA. Opt. Lett. 2009; 34:2961–2963. [PubMed: 19794782]
28. Swaroop A, Xu JZ, Pawar H, Jackson A, Skolnick C, Agarwal N. Proc. Natl. Acad. Sci. USA. 1992; 89:266–270. [PubMed: 1729696]
29. Mears AJ, Kondo M, Swain PK, Takada Y, Bush RA, Saunders TL, Sieving PA, Swaroop A. Nat. Genet. 2001; 29:447–452. [PubMed: 11694879]
30. Akimoto M, Cheng H, Zhu D, Brzezinski JA, Khanna R, Filippova E, Oh EC, Jing Y, Linares JL, Brooks M, Zareparsi S, Mears AJ, Hero A, Glaser T, Swaroop A. Proc. Natl. Acad. Sci. USA. 2006; 103:3890–3895. [PubMed: 16505381]
31. Liu X, Grishanin RN, Tolwani RJ, Rentería RC, Xu B, Reichardt LF, Copenhagen DR. Neurosci. 2007; 27:7256–7267.
32. Feng L, Xie X, Joshi PS, Yang Z, Shibasaki K, Chow RL, Gan L. Development. 2006; 133:4815–4825. [PubMed: 17092954]
33. Hammer M, Roggan A, Schweitzer D, Muller G. Phys. Med. Biol. 1995; 40:963–978. [PubMed: 7659735]
34. Jeon CJ, Strettoi E, Masland RH. J. Neurosci. 1998; 18:8936–8946. [PubMed: 9786999]
35. Rozanowski B, Burke JM, Boulton ME, Sarna T, Rózanowska M. Invest. Ophthalmol. Vis. Sci. 2008; 49:2838–2847. [PubMed: 18326697]
36. Zarbin MA. Arch. Ophthalmol. 2004; 122:598–614. [PubMed: 15078679]
37. Yu DY, Cringle SJ. Prog. Retin. Eye. Res. 2001; 20:175–208. [PubMed: 11173251]
38. Wenzel A, Grimm C, Samardzija M, Remé CE. Prog. Retin. Eye. Res. 2005; 24:275–306. [PubMed: 15610977]
39. Wright AF, Chakarova CF, Abd El-Aziz MM, Bhattacharya SS. Nat. Rev. Genet. 2010; 11:273–284. [PubMed: 20212494]

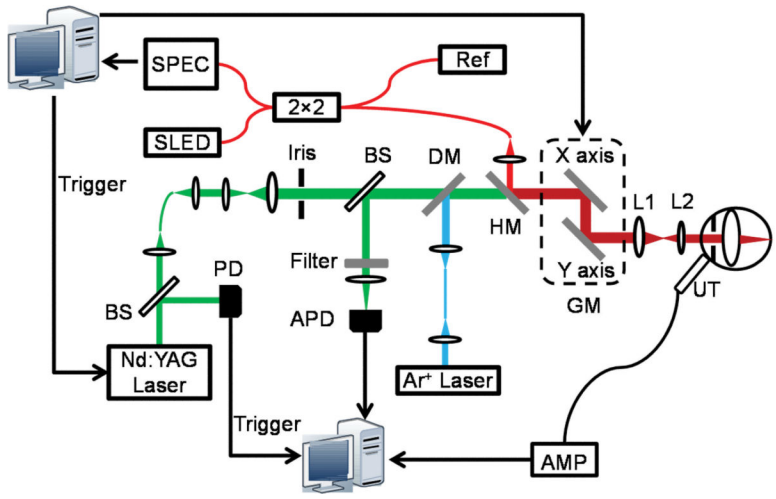

Figure 1.

Schematic diagram of the multimodal retinal imaging system. SLED: superluminescent laser diode; Ref: OCT reference arm; 2×2: 50:50 optical fiber coupler; SPEC: spectrometer; BS: beam splitter; DM: dichroic mirror; HM; hot mirror; GM: 2D galvanometer mirrors; AMP: amplifier; UT: ultrasonic transducer; PD: photodiode; APD: avalanche photodetector.

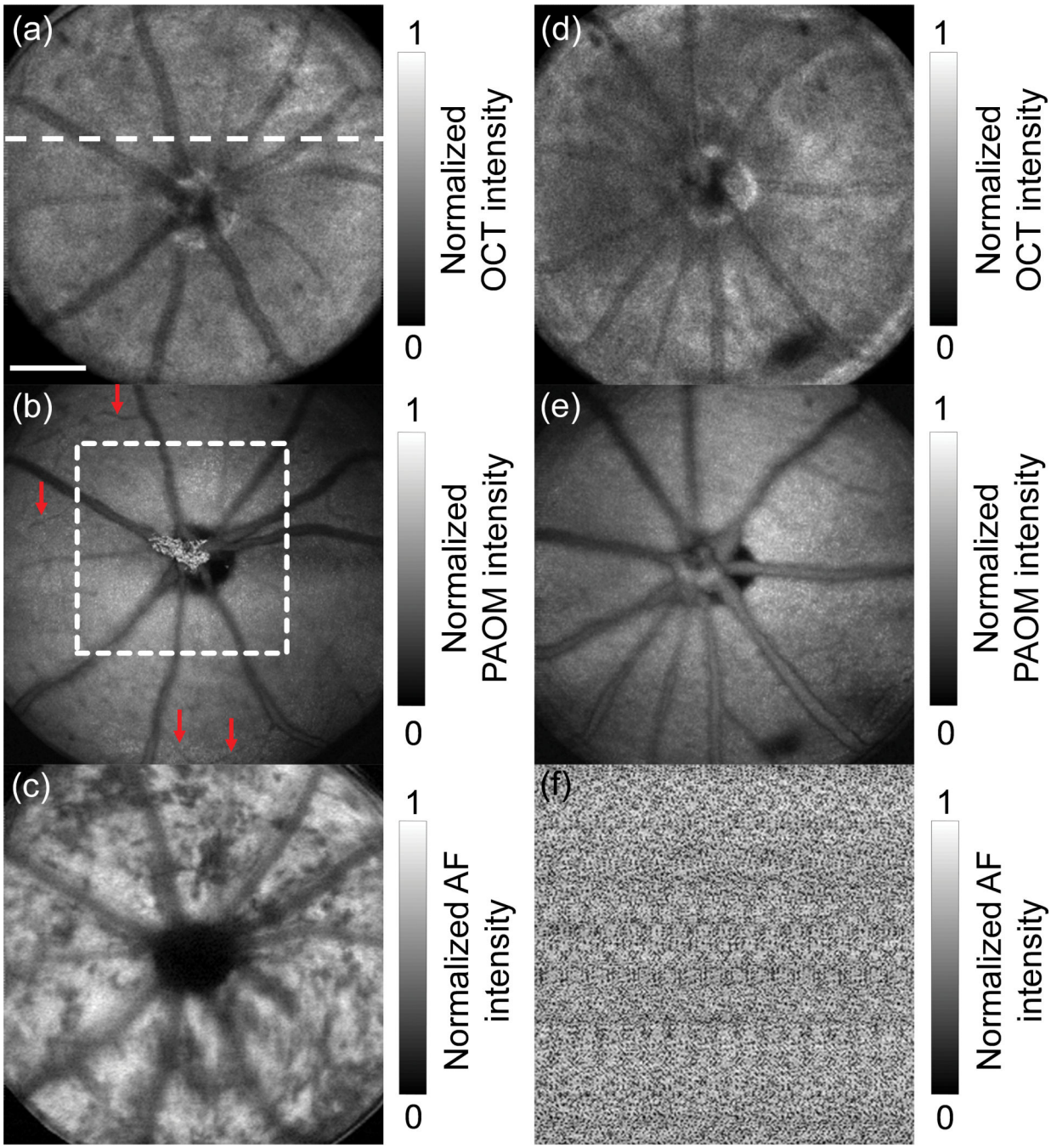

Figure 2.

In vivo multimodal retinal imaging. (a) and (d) are *en face* SD-OCT images; (b) and (e) are PAOM fundus images; (c) and (f) are AF-SLO fundus images. The images on the left are acquired from a transgenic Nrl-GFP mouse and the images on the right are acquired from a control mouse. The arrows in Figure 2b point out some smaller vessel shadows that were visible in PAOM but invisible in SD-OCT and AF-SLO. Bar: 300 μm.

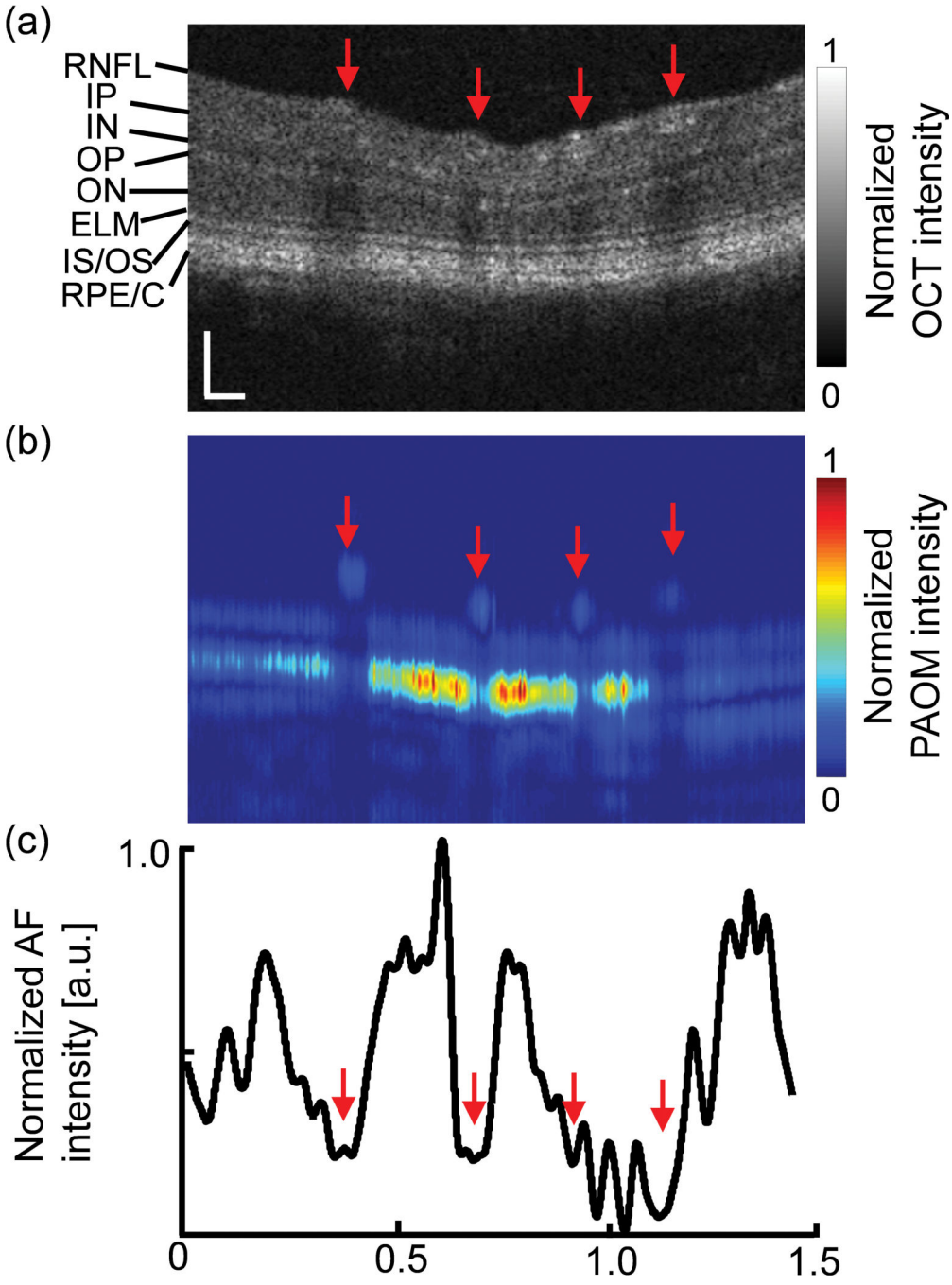

Figure 3.

Comparison of (a) SD-OCT cross-section, (b) PAOM B-scan, and (c) 1D AF-SLO profile acquired from the same position. RNFL/GC: retinal nerve fiber layer and ganglion cell layer; IP: inner plexiform layer; IN: inner nuclear layer; OP: outer plexiform layer; ON: outer nuclear layer; ELM: external limiting membrane; IS/OS: the inner and outer segment of the photoreceptors; RPE/C: the complex of retinal pigment epithelium and choroid. The arrows pointing out the four retinal vessels show good registration among the three imaging modalities. Bar: 100 μm.

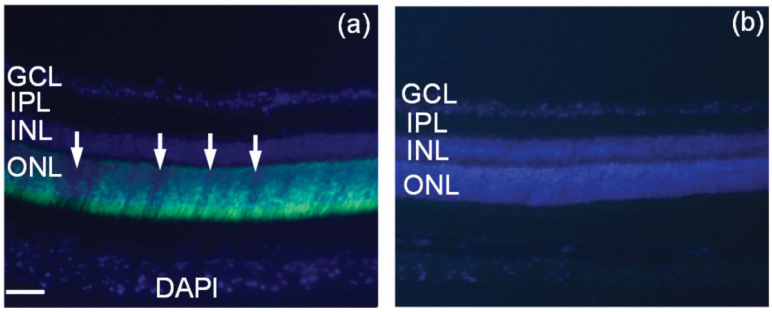

Figure 4.

Retinal histological of the (a) GFP-expressing eye and the (b) control eye. The anatomic retinal layers were resolved by DAPI staining (blue) in both eyes. The turquoise band locates in ONL represents GFP expression. GCL: ganglion cell layer; IPL: inner plexiform layer; INL: inner nuclear layer; ONL: outer nuclear layer. The locations pointed out by arrows indicate no GFP expression. Bar: 50 μm.

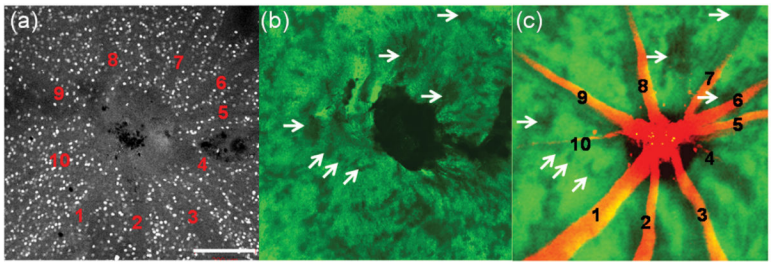

Figure 5.

Comparison between *ex vivo* flat-mount confocal microscopy results and the *in vivo* results. (a) Confocal microscopy of the whole-mount retina stained by Brn-3b. The trace of major retinal vessels is labeled by numbers. (b) Confocal microscopy of GFP expression in the whole-mount retina. The photoreceptors with GFP expression appeared as bright turquoise regions. (c) Overlaid *in vivo* PAOM and AF-SLO images within the region highlighted by the dashed-box in Figure. 2b. The retinal vessels in PAOM are pseudo-colored in red and the AF-SLO image is pseudo-colored in green. Representative photoreceptors in absence of GFP were highlighted by arrows. Bar: 100 μm.